

# A Cyclic Nano-reactor Achieving Enhanced Photodynamic Tumor Therapy by Reversing Multiple Resistances

**Peng Liu**

Central South University

**Yanbin Zhou**

Central South University

**Xinyi Shi**

Central South University

**Yu Yuan**

Central South University

**Ying Peng**

Central South University

**Qiange Luo**

Central South University

**Jinsong Ding**

Central South University

**Yong Li**

Hunan Children's Hospital

**Wenhu Zhou** (✉ [zhouwenhuyaoji@163.com](mailto:zhouwenhuyaoji@163.com))

Central South University

---

## Research

**Keywords:** Nanomedicine, targeting, tumor hypoxia, drug resistance, starvation therapy, GSH depletion, oxygenation, metal-organic-frameworks

**Posted Date:** February 23rd, 2021

**DOI:** <https://doi.org/10.21203/rs.3.rs-225544/v1>

**License:**   This work is licensed under a Creative Commons Attribution 4.0 International License.

[Read Full License](#)

---

# Abstract

**Background:** Photodynamic therapy (PDT) is a clinically implemented modality to combat malignant tumor, while its efficacy is largely limited by several resistance factors from tumor microenvironment (TME), such as hypoxia, anti-oxidant systems, and ATP-dependent tumor adaptive resistances. Considering the complexity of tumor, simultaneously remodeling multiple TME is preferred to revitalize the PDT for enhanced cancer treatment.

**Results:** Here, a targeting nano-reactor was facilely constructed to reverse the multiple resistances of PDT by incorporating glucose oxidase (GOx) and chlorin e6 (Ce6) into poly (D, L-lactic-co-glycolic acid) (PLGA)/ metal-organic framework (MOF) core-shell nanoassembly, with surface deposition of hyaluronic acid (HA) stabilized MnO<sub>2</sub>. The nano-reactor could selectively target tumor cells by virtue of surface HA modification, and once internalization, a few reactions were initiated to modulate TME. Glucose was consumed by GOx to inhibit ATP generation, and the produced H<sub>2</sub>O<sub>2</sub> was catalyzed by MnO<sub>2</sub> to generate O<sub>2</sub> for tumor hypoxia alleviation and photodynamic sensitization, and glutathione (GSH) was also effectively depleted by MnO<sub>2</sub> to suppress the tumor antioxidant defense. Consequently, the nano-reactor achieved robust PDT with amplified tumor therapy via intravenous injection.

**Conclusions:** This nano-reactor offers a multifunctional nanoplatform to sensitize TME-limited tumor treatment means via reversing multiple resistances.

## Background

Photodynamic therapy (PDT) has gain tremendous fundamental and translational attention for tumor therapy, owing to its advantages of low systemic toxicity, non-invasive, spatial and temporal controllable activation.<sup>1-2</sup> During the process of PDT, the photosensitizers (PSs) are activated by light to convert oxygen into toxic reactive oxygen species (ROS), which bind and dis-functionalize some bio-macromolecules in tumor cells, such as DNA and lipid, resulting in cell apoptosis or necrosis, immune responses and microvascular damage.<sup>3-6</sup> Such process is highly efficient to kill cancer at cellular level, and some PSs, such as verteporfin, 5-ALA and temoporfin, have been demonstrated as promising candidate for clinical translation.<sup>7-8</sup> However, while PDT has been accepted for several types of cancer in clinic,<sup>9</sup> its widespread implementation are still hindered by various biological limitations. Aside from the inherent barrier of light penetration that can be partially addressed by deep PDT techniques, tumor resistances are the main mechanism to weaken the efficacy of PDT.<sup>10</sup>

Tumor cells can resist PDT by different pathways due to the complexity of tumor microenvironment (TME), in which the most well-known feature is hypoxia. Hypoxic cells are ~3-fold more resistant to ROS damage than aerobic cells,<sup>11</sup> and more importantly, hypoxic environment could directly decrease the PDT efficacy by blocking the oxygen supply.<sup>12-13</sup> What's more, the PDT process would further aggravate tumor hypoxia through oxygen consumption and vascular damage, which activates hypoxia inducible factor-1α

(HIF-1 $\alpha$ ) survival pathway, thus causing PDT resistance.<sup>14-15</sup> At the same time, cancer cells are equipped with antioxidant defense systems, in which the most abundant one is glutathione (GSH), to scavenge the ROS and thus counteract ROS-mediated injury.<sup>16-18</sup> In addition, tumor cells could generate adaptive resistance toward PDT through upregulation of drug efflux proteins, heat shock proteins (HSPs), and DNA repair proteins.<sup>19-21</sup> It has been reported that numerous drug efflux proteins, such as P-glycoprotein (P-gp), and ATP-binding cassette super-family G member 2 (ABCG2), have been implicated in PDT resistance via pumping out PSs before their action.<sup>22</sup>

To reverse PDT resistance, various nano-systems capable of modulating TME have been developed. For example, replenishment of oxygen is a commonly employed strategy to alleviate hypoxia, which can be achieved by either oxygen delivery (using hemoglobin or perfluorocarbons) or endogenous oxygen generation (through catalytic converting tumor abundant H<sub>2</sub>O<sub>2</sub> into O<sub>2</sub>).<sup>23-25</sup> Oxygen generation can be further boosted by cascade equipping the nano-system with glucose oxidase (GOx) to supplement H<sub>2</sub>O<sub>2</sub> substrate.<sup>26</sup> To augment PDT efficacy, several nano-vehicles were also designed to suppress the tumor antioxidant defense and restore the ROS damage effect of PDT via antioxidants depletion.<sup>27-28</sup> Moreover, inhibition of ATP was reported to sensitize PDT by inhibiting drug efflux and aggravating PDT-induced DNA damage.<sup>29-30</sup> Ideally, simultaneous remodeling various TME to alleviate multiple biological resistances is preferred for optimized PDT, considering the cunning nature of cancer. Unfortunately, the development of nanoparticles with multifunctionalities often requires sophisticated materials design and complicated preparation procedure, thus imposing the difficult of cost-effective, reproducible, and scalable production.

To tackle this, we designed and facilely prepared a core-shell nano-reactor for enhanced PDT via simultaneous oxygenation, antioxidant suppression, and ATP depletion (Scheme 1). Tannic acid (TA), ferric iron (Fe<sup>3+</sup>) and poly (D, L-lactic-co-glycolic acid) (PLGA) were assembled into core-shell structure via hydrophobic,  $\pi$ - $\pi$  staking, and electrostatic interactions,<sup>31-32</sup> in which chlorin e6 (Ce6, a widely used PS) and GOx was co-loaded. MnO<sub>2</sub> was deposited on particle surface and stabilized by hyaluronic acid (HA) through layer-by-layer electrostatic adsorption. In our system, the MnO<sub>2</sub> played dual roles of self-oxygen supply and GSH depletion via its catalase-mimic activity and oxidibility, respectively. The GOx boosted the oxygenation by in-situ generation of H<sub>2</sub>O<sub>2</sub>, and its capability of glucose consumption blocked the energy supply to decrease ATP generation. All these functions collectively remodeled the TME from different aspect to sensitize PDT efficacy, which has been demonstrated by solution, in vitro and in vivo experimental results. The nanosystem could passively accumulate into tumor, actively internalize tumor cells via HA-mediated targeting, and impose potent PDT effect via reversing multiple resistances.

## Materials And Methods

### Materials

Chlorin e6 (Ce6) and Nile red (NR) were obtained from Frontier Scientific, Inc. (Utah, USA). PLGA (Mw: 20 kDa) was purchased from Daigang Biomaterial Co., Ltd. (Jinan, China). Hyaluronic acid (HA, 7 kDa) was purchased from Lifecore Biomedical Company (MN, USA). Poly (allylamine hydrochloride) (PAH), tannic acid (TA), glucose oxidase (GOx), singlet oxygen sensor green (SOSG), and 3-(4, 5-dimethylthiazol-2-yl)-2, 5-diphenyl tetrazolium bromide (MTT) were provided by Sigma-Aldrich (Saint Louis, MO, USA). Live & dead viability/cytotoxicity assay kit was obtained by Invitrogen (NY, USA), and 4', 6-diamidino-2-phenylindole (DAPI) was provided by Solarbio Biotech, Co., Ltd. (Beijing, China). Ferric chloride hexahydrate ( $\text{FeCl}_3 \cdot 6\text{H}_2\text{O}$ ), N-acetylcysteine (NAC) and 2' 7'-dichlorofluorescein diacetate (DCFDA) were obtained from Sinopharm Chemical Reagent Co., Ltd (Shanghai, China). DMEM medium, fetal bovine serum, streptomycin/penicillin and Trypsin-EDTA were provided by GIBCO (NY, USA). DNS reagent was purchased from Coolaber Biotech, Co., Ltd. (Beijing, China). ROS-ID hypoxia detection kit was provided by Enzo Life Sciences Inc. (NY, USA).

### **Preparation of PTFCG@MH**

Ce6,  $\text{FeCl}_3$  and PLGA were mixed in acetone at a concentration of 400  $\mu\text{g}/\text{mL}$ , 400  $\mu\text{g}/\text{mL}$  and 2 mg/mL, respectively. Then, 1 mL of such mixture was added dropwise to 5 mL aqueous solution containing 320  $\mu\text{g}/\text{mL}$  TA and 20  $\mu\text{g}/\text{mL}$  GOx under constant sonication. The solution was stirred at 30 °C for 3 h to evaporate acetone. The PTFCG was separated by centrifugation (16000 rpm, 25 min) and washed by deionized water. To prepare PTFCG@MH, 50  $\mu\text{L}$  PAH (20 mg/mL) was mixed with 1 mL PTFCG solution and mild stirred for 30 min. Then, 25  $\mu\text{L}$  potassium permanganate (10 mg/mL) was added and stirred for another 1 h. After centrifugation (16000 rpm for 25 min) and washing with deionized water, the PTFCG@M was obtained. Finally, 500  $\mu\text{L}$  HA (20 mg/mL) was introduced into 1 mL of PTFCG@M solution and stirred for 1 h. Excess HA was removed by centrifugation, and PTFCG@MH was collected.

### **Characterizations of PTFCG@MH**

The particle sizes and  $\zeta$  potential were measured by a Malvern Zeta Sizer Nano series (Malvern, UK). The morphologies and element analysis were recorded on a TEM-EDS (Titan G2 60-300, FEI, USA). The UV-vis absorption spectra were carried out on UV-visible spectrophotometer (Shimadzu, Japan). The fluorescence spectra were collected using FL-2700 spectrofluorometer (HITACHI). The Ce6 concentration was determined by the UV-visible spectra method, and the loading amount of GOx was estimated using BCA protein assay (Beyotime).

### ***In vitro* release of Ce6**

The PTFCG@MH solution ([Ce6] = 200  $\mu\text{g}/\text{mL}$ ) was dispersed in 5 mL of various dissolution media. The mixtures were shaken gently in a shaking incubator at 37 °C. At predetermined time intervals, the samples were withdrawn and centrifuged. The supernatant was collected, and the amount of Ce6 was quantified by UV absorbance quantification ( $\lambda = 640 \text{ nm}$ ).

### **Cyclic reaction of PTFCG@MH**

The catalytic activity of GOx was determined by measuring the glucose consumption and pH change in presence of glucose. The PTF@MH, PTFCG or PTFCG@MH solution (4 µg/mL GOx) was mixed with glucose (10 mM) at 37 °C in the presence or absence of H<sub>2</sub>O<sub>2</sub>. Then, the glucose concentration and pH value were measured by DNS reagent and a pH meter (PHSJ-4F, INESA, China), respectively. To monitor the oxygen generation under different acidic conditions, PTFCG@MH was dispersed in PBS (pH 5.0, 6.0, and 7.0) containing 1 mM H<sub>2</sub>O<sub>2</sub>. At predetermined time points, the dissolved O<sub>2</sub> was detected using the portable dissolved oxygen meter (JPBJ-609L, INESA, China). To monitor the self-oxygen balance, glucose (10 mM) and H<sub>2</sub>O<sub>2</sub> (100 µM) were added, and the dissolved O<sub>2</sub> was measured with or without laser irradiation.

### **The <sup>1</sup>O<sub>2</sub> generation analysis**

PTFCG@MH or PTF@MH (1 µg/mL Ce6) was added into SOSG solution (2.5 µM), followed by adding H<sub>2</sub>O<sub>2</sub> (10 mM). Then, a continuous laser (100 mW/cm<sup>2</sup>, 635 nm) was performed at predetermined time points, and fluorescence intensity was detected immediately by fluorescence spectroscopy (Ex = 490 nm, Em = 525 nm).

### **Cellular uptake**

The NR-loaded nanoparticles were prepared following the method described above by replacing Ce6 with NR. The cells were seeded in Petri dish (35 mm) at 5 × 10<sup>4</sup> cells/cm<sup>2</sup> and cultured overnight. With or without pre-treatment of free HA (10 mg/mL) for 1 h, the cells were incubated with NR-loaded nanoparticles or free NR for another 2 h. Next, the cells were washed with pre-cooled PBS and fixed with 4% paraformaldehyde. After staining by DAPI, the cells were imaged under confocal microscope (LSM780 NLO, Zeiss, Germany).

### **Intracellular O<sub>2</sub> consumption and ROS detection**

ROS-ID and DCFDA were used to detect the intracellular O<sub>2</sub> consumption and ROS generation inside cells. The MDA-MB-231 cells were seeded in 24-well culture plate (10<sup>5</sup> cells/well). After sealing by liquid paraffin, the cells were incubated with PTFCG@MH, PTF@MH, PTFCG, or free Ce6 (1 µg/mL Ce6) for 2 h. Then, laser irradiation (635 nm, 100 mW/cm<sup>2</sup>) was applied for 2 min. With PBS washing for three times, the mixture of ROS-ID (0.5 µM) and DCFDA (10 µM) was added into each group for 30 min further incubation. After washing with pre-cooled PBS, fluorescence inside cells was observed by fluorescence imaging system (NIKON, Ti-S, Japan).

### **Intracellular ATP and GSH detection**

MDA-MB-231 cells were seeded in 12-well plate at a density of 2 × 10<sup>5</sup> cells per well for 12 h incubation. Then, various formulations with different concentrations were added for 24 h incubation. After that, the cells were collected and lysed using ATP lysis buffer, and ATP concentration was measured by ATP assay

kit (Beyotime). Likewise, the cells were collected and lysed using the Triton-X 100 cell lysis buffer, and GSH concentration was detected by the Ellman's reagent. The numbers of cells were standardized by measuring total protein concentration using BCA protein assay.

### ***In vitro* cytotoxicity studies**

MDA-MB-231 cells were seeded in a 96-well plate (5000 cells/well) for overnight incubation. The cells were treated with PTFCG or PTFCG@MH at different concentrations for 24 h, followed by laser irradiation for 1 min (100 mW/cm<sup>2</sup>, 635 nm). After 24 h, MTT solution (1 mg/mL) was added for another 4 h incubation. The medium was replaced with 100 µL of DMSO. The absorbance values were recorded to calculate the cell viability. Then, the Live/Dead assay was carried out by calcein AM/propidium iodide double staining. The cells were seeded and treated as described above. After laser irradiation, the fresh medium containing calcein AM/propidium iodide was added for 20 min incubation. Finally, the cells were imaged by fluorescence imaging system (NIKON, Ti-S, Japan).

### ***In vivo/ex vivo* fluorescence imaging**

Healthy female Balb/c mice (aged 4-6 weeks) were purchased from the Laboratory Animal Center of Central South University. All experimental procedures were carried out in accordance with the Regulations for the Administration of Affairs Concerning Experimental Animals of China, and approved by the Ethics Committee for Research in Animal Subjects at Xiangya School of Pharmaceutical Sciences of Central South University. MDA-MB-231 tumor-bearing mice were obtained by subcutaneously injecting a cells suspension in PBS (10<sup>6</sup> cells) into the right armpit of mice. When the tumor volume reached ~100 mm<sup>3</sup>, the mice were treated with different formulations.

For *in vivo/ex vivo* imaging, the tumor-bearing mice were intravenously injected with free Ce6 or PTFCG@MH (100 µL, 2.5 mg/kg Ce6), and the fluorescence images were taken by an optical imaging system (IVIS Lumina, PerkinElmer, USA) at 1 h and 24 h post-injection. The mice were sacrificed at 24 h after injection, and the major organs were collected for *ex vivo* imaging. The images were analyzed using Living Imaging Software (IVIS Lumina LT, PerkinElmer, USA).

### ***In vivo* antitumor study**

The tumor-bearing mice were randomly divided into 5 groups and injected intravenously with (1) PBS, (2) Ce6 + Laser, (3) PTFCG + Laser, (4) PTFCG@MH, (5) PTFCG@MH + Laser (100 µL, 2.5 mg/kg Ce6) at day 0 and 4. The irradiation groups were exposed to laser (100 mW/cm<sup>2</sup>, 635 nm) for 5 min at 24 h after injection. The tumor volume was recorded and calculated as follows:  $V = (\text{length} \times \text{width}^2)/2$ . In addition, the body weights were also obtained. At day 14, all the mice were sacrificed, and the tumors and major organs were collected. The tumors were weighed and photographed using a high-quality camera. For histology analysis, the major organs and tumors were extracted and immersed in 4% formaldehyde, embedded in paraffin, sectioned, stained with H&E and observed by an optical microscope. To evaluate HIF-1α level, the tumor tissues were dissected for HIF-1α immunofluorescence staining assay.

# Results And Discussion

## Nanoparticles preparation and characterization

The GOx and Ce6 were co-loaded into nanocomposites (PTFCG) using a solvent exchange and evaporation method (Scheme 1), in which the ethanol solution (containing Ce6, PLGA and  $\text{FeCl}_3$ ) was dropwise added into the aqueous phase (with TA and GOx). During organic evaporation, the TA-Fe metal-organic frameworks (MOFs) were coated on the surface of hydrophobic PLGA nano-core for particle stabilization, and the resulting PTFCG displayed a dynamic diameter of  $\sim 175$  nm (Figure 1A, Figure S1) with  $\zeta$  potential of  $-33.4$  mV (Figure 1C). From the TEM image, the PTFCG displayed a roughly spherical morphology with an obvious core-shell structure (inset in Figure 1A). To further deposit  $\text{MnO}_2$  on particle surface, a  $\text{KMnO}_4$  solution was added, followed by adding PAH to reduce  $\text{KMnO}_4$ , allowing for in-situ growth of  $\text{MnO}_2$  on nanoparticle surface to yield PTFCG@M. Compared with PTFCG, the  $\zeta$  potential of PTFCG@M was reversed to positive ( $+17.3$  mV) (Figure 1C), which allowed for the subsequent HA coating via electrostatic attraction (termed PTFCG@MH). The successful HA modification was evidenced by the decrease of particle charge to negative ( $-21.7$  mV) (Figure 1C). The resulting PTFCG@MH nanoparticles displayed a dynamic diameter of  $\sim 205$  nm (Figure 1B), while the size measured by TEM was  $\sim 160$  nm (inset in Figure 1B, Figure S2). It is reasonable as DLS measurement would distort the particle size being observed due to the particle surface hydration. Importantly, the HA modification not only significantly increased the colloidal stability (Figure S3), but also rendered the nanoparticles with tumor targetability (vide infra).

According to the UV-vis absorbance spectra, PTFCG had characteristic Ce6 peaks at 404 nm and 640 nm, indicating the successful Ce6 loading (Figure 1D). For PTFCG@MH, a wide absorbance band in the range from 250-400 nm appeared, which was ascribed to the  $\text{MnO}_2$ . To confirm the  $\text{MnO}_2$  coating, the energy dispersive X-Ray spectroscopy (EDS) was conducted, and a high Mn element content ( $\sim 6\%$ ) was observed (Figure 1E). The drug loading for Ce6 and GOx was measured to be  $108.4$   $\mu\text{g}$  and  $24.6$   $\mu\text{g}$  per mg of PTFCG@MH, respectively. Interestingly, after encapsulation into nanoparticles, the intrinsic fluorescence of Ce6 was significantly quenched, especially for PTFCG@MH (Figure S4). However, such quenched fluorescence can be largely recovered upon addition of GSH, indicating GSH-responsive release of Ce6. To confirm this, Ce6 release behavior from PTFCG@MH was investigated (Figure 1F). In absence of GSH, the Ce6 showed  $\sim 20\%$  accumulative release, while a burst drug release was observed after adding GSH, with  $\sim 60\%$  Ce6 release within 8 h. Therefore, such nanosystem showed a triggered activation of photodynamic activity in response to intracellular stimulus, thus minimizing the potential phototoxicity of Ce6 during *in vivo* delivery.

## A cyclic reaction nano-reactor

As illustrated in Figure 2A, our nanosystem was designed with a few cyclic reactions to enhance the Ce6-based PDT. GOx consumes glucose (Glu) to block the energy (ATP) supply, and the concomitantly produced  $\text{H}_2\text{O}_2$  is decomposed by the catalase-mimic  $\text{MnO}_2$  to generate  $\text{O}_2$ , which in turn boosts the  $^1\text{O}_2$  production under laser illumination. To demonstrate this concept, each reaction was tested individually.

The catalytic activity of GOx was first measured by monitoring the glucose consumption (Figure 2B). After 60 min incubation, PTFCG@MH decreased the glucose level by 34%, while the nanoparticles without GOx loading (termed PTF@MH) did not show any glucose consumption. Therefore, GOx maintained its catalytic activity after being loaded into nanoparticles. The activity of GOx can also be monitored by the pH decrease due to the generation of gluconic acid byproduct. Upon addition of glucose, both PTFCG and PTFCG@MH showed a gradual pH decrease over time (Figure 2C). Notably, PTFCG@MH exhibited a relative lower pH decrease rate than that of PTFCG. This is likely due to that the surface deposited  $\text{MnO}_2$  impeded accessibility of glucose into GOx-loaded nanocore. In addition, the  $\text{MnO}_2$  could neutralize  $\text{H}^+$  to slow down pH decrease rate.

Next, the catalase-mimic activity of  $\text{MnO}_2$  was tested by monitoring  $\text{O}_2$  production in presence of  $\text{H}_2\text{O}_2$  (Figure 2D). As a control, the PTFCG@MH alone did not show any  $\text{O}_2$  generation. However, a rapid increase of the dissolved  $\text{O}_2$  was observed upon addition of  $\text{H}_2\text{O}_2$ . We also studied the effect of pH, and a marginal increase of catalytic rate was seen with the decrease of pH from 7.0 to 5.0. Overall, the catalytic efficiency was relatively higher under acidic tumor microenvironment than physiological conditions.

After confirming the single catalytic reaction of GOx and  $\text{MnO}_2$ , we next explored the catalytic circulation by measuring the oxygen variation (Figure 2E). For PTFCG, the dissolved  $\text{O}_2$  was quickly decreased within 100 s upon addition of glucose. For the PTFCG@MH, by contrast, the  $\text{O}_2$  consumption rate significantly lessened due to the self-oxygen generation activity of  $\text{MnO}_2$ , demonstrating the cyclic oxygen supply. Moreover, the  $\text{O}_2$  balance was achieved upon further addition of  $100 \mu\text{M}$   $\text{H}_2\text{O}_2$  (which mimics the tumor microenvironment),<sup>33</sup> and such  $\text{O}_2$  generation efficiency is strong enough to support the PDT (Figure 2E, blue trace). In addition, extra addition of  $\text{H}_2\text{O}_2$  also accelerated the glucose consumption as shown in Figure 2B (black trace).

With cyclic oxygen supply, we next explored the enhanced PDT effect by measuring the single oxygen ( $^1\text{O}_2$ ) generation using singlet oxygen sensor green (SOSG) as a fluorescent indicator (Figure 2F). In presence of  $\text{H}_2\text{O}_2$ , the production of  $^1\text{O}_2$  was obviously increased for PTFCG@MH, and the addition of glucose could also strengthen the PDT effect. As a control, the PTFCG group showed lower  $^1\text{O}_2$  generation due to the lack of oxygen supply. All these results demonstrated the capability of cyclic nano-reactor for boosting PDT effect of Ce6.

## Cellular uptake

We next tested the intracellular performance of the nanosystem by using MDA-MB-231 cancer cells. To track the intracellular delivery, nanoparticles were labeled with a red fluorescent Nile red (NR), and the cell nuclei were stained blue by DAPI for localization (Figure 3A). From confocal laser scanning microscopy (CLSM) images, a weak red signal was observed when the cells were treated with free NR, while the fluorescence was significantly intensified for nanoparticles. From the merged image, the fluorescence of nanoparticles mainly distributed in the cytoplasm, indicating endocytosis pathway for internalization. To demonstrate tumor targetability of such surface HA modified nanosystem, the cells were pretreated with free HA to saturate the CD44 binding, and in this case the intracellular nanoparticles signal decreased obviously. We also quantified the contribution of HA-mediated internalization by measuring the intensity of each treatment, where the uptake was significantly decreased upon free HA pre-treatment (Figure 3B). These results confirmed that our nanosystem was able to selectively recognize tumor cells via CD44 receptor for targeting delivery.

### **Enhanced anti-tumor efficacy via hypoxia alleviation and ATP/GSH depletion**

After internalization, we next explored the intracellular functions of the nanosystem. To visualize the PDT effect, the ROS generation was probed by using 2' 7'-dichlorofluorescein diacetate (DCFDA) indicator. Interestingly, both PTF@MH and PTF@MH could scavenge the intracellular ROS to some extent as compared to the control, due to the catalase activity of  $\text{MnO}_2$ . Upon irradiation, each Ce6-based formulation showed enhanced green fluorescence inside cells based on both fluorescent images (Figure 4A) and quantified intensity (Figure 4B). Notably, PTF@MH group emit the strongest fluorescence, indicating the best PDT efficacy. This can partially be explained by the cyclic oxygenation of the nano-reactor for self-oxygen supply. To confirm this, we then measured the  $\text{O}_2$  balance by using a red fluorescent hypoxia detection kit. Both PTF@MH and PTF@MH could relieve tumor hypoxia with red fluorescence decrease compared to non-treatment control (Figure 4A, 4C), also attributable to self-oxygen supply of the  $\text{MnO}_2$ . Upon addition of laser, the hypoxia was strongly exacerbated for free Ce6 and PTF@MH groups, ascribed to PDT- and GOx-based oxygen consumption. However, the PTF@MH group showed low hypoxia level even after laser irradiation. Therefore, such nano-reactor is robust enough to maintain oxygen balance with enhanced PDT efficacy.

Besides cyclic oxygen supply, such nano-reactor was also designed to deplete both ATP and GSH. We next tested these properties by measuring the intracellular ATP and GSH levels using ATP assay kit and Ellman's reagent, respectively. Because of catalytic glucose oxidation, free GOx could effectively decrease ATP level in a concentration dependent manner by blocking the energy supply (Figure 4D). Likewise, the PTF@MH could also inhibit ATP generation, while the PTF@MH did not show any activity due to the absence of GOx loading.  $\text{MnO}_2$  is a well-known GSH depletor due to its capability to oxidize GSH into GSSG, accompanied by its reduction into  $\text{Mn}^{2+}$ .<sup>27, 34</sup> As expected, the PTF@MH with  $\text{MnO}_2$  doping displayed high efficient GSH depletion, with over 80% GSH decrease at 5  $\mu\text{g}/\text{mL}$  NPs (Figure 4E). Note that ATP is the basic energy source for tumor cells to acquire treatments resistance including PDT

therapy,<sup>35</sup> and GSH could directly scavenge  $^1\text{O}_2$  to alleviate the PDT efficacy. Therefore, with ATP and GSH dual-depletion activity, such nano-reactor was expected to enhance the PDT-based anti-tumor activity via distinct mechanisms.

Next, the *in vitro* cytostatic activity of nanosystem was evaluated by MTT assay. Without drugs loading, the PTF and PTF@MH showed satisfactory biocompatibility even at high concentrations (Figure S5). The PTFCG, on the other hand, displayed a concentration-dependent tumor ablation activity (Figure 4F), ascribed to the starvation therapy for ATP depletion.<sup>36</sup> Upon laser irradiation, the antitumor effect was further enhanced. Notably, PTFCG@MH showed significantly better efficacy than PTFCG attributable to  $\text{MnO}_2$  doping for self-oxygen circulation, GSH depletion, as well as HA modification for targeting delivery. We also explored the cell death pathway by co-staining the cells using calcein-AM (green fluorescence for live cells) and propidium iodide (red fluorescence for dead/late apoptotic cells). After different treatments, green fluorescence was weakened while the red fluorescence became intensified inside cells (Figure 4G), indicating an apoptotic cell death mechanism. In addition, the general anti-tumor activity for each treatment was highly consistent with the results from MTT assay.

### ***In vivo* performance of the nano-reactor**

Finally, *in vivo* behavior of the nano-reactor was explored by using MDA-MB-231 tumor-bearing mice. By virtue of the intrinsic fluorescence of Ce6, the bio-distribution was visualized using a living imaging system. PTFCG@MH or free Ce6 was intravenously injected when the tumor volume reached  $\sim 100 \text{ mm}^3$ . At 1 h post-injection, Ce6 showed red fluorescence throughout the body (Figure 5A), indicating non-specific distribution, while most of the fluorescence was cleared after 24 h, with major accumulation in liver. For comparison, the PTFCG@MH displayed much weaker fluorescence at 1 h post-injection due to the fluorescence quenching of the nanosystem, further demonstrating its advantage for decreased phototoxicity. However, the signal at tumor tissue became intensified after 24 h circulation (Figure 5A, black circle), indicating the EPR effect of the nanomedicine for passive accumulation into tumor. We then quantified the results by collecting the main organs as well as tumor tissues for *ex vivo* fluorescence imaging (Figure 5B). PTFCG@MH exhibited  $\sim 3.7$ -fold higher intensity at tumor site than free Ce6, confirming the targetability of the nanosystem towards tumor tissue.

To evaluate the *in vivo* tumor ablation activity, the tumor bearing mice were randomly divided into five groups (n = 5), each intravenous injection of PBS, Ce6 + Laser, PTFCG + Laser, PTFCG@MH, and PTFCG@MH + Laser, respectively (100  $\mu\text{L}$ , 2.5 mg/kg Ce6), with totally two injections (day 0 and day 4). The laser was performed at 24 h after injection. The therapeutic efficacy was monitored by measuring the tumor size every other day (Figure 5C). Compared with PBS control, free Ce6 only showed marginal tumor growth inhibition, mainly due to its rapid clearance from mouse body with minimal accumulation into tumor tissue (Figure 5A). While the nanoparticles could facilitate tumor targeting delivery of Ce6, the efficacy of PTFCG plus laser irradiation was still poor, due to the multiple resistance mechanisms of

tumor against PDT therapy. For PTFCG@MH, by contrast, the efficacy was strongly enhanced. Note that without laser irradiation, the therapeutic effect of PTFCG@MH was also rather limited, verifying that the anti-tumor activity was mainly originated from the PDT effect.

Next, the tumor tissues were extracted for a series of characterizations. Based on the photographs and tumor weight evaluations (Figure 5D), it was clearly seen that PTFCG@MH plus laser achieved the best efficacy, in consistent with the *in vivo* measurement. Such results were further confirmed by H&E staining (Figure 5E), in which the highest level of cell necrosis was observed in PTFCG@MH plus laser group. We also evaluated the key pathological feature of tumor hypoxia by immunofluorescence staining of HIF-1 $\alpha$ . The solid tumor showed a relatively high-level HIF-1 $\alpha$  expression due to its hypoxia microenvironment (Figure 5F), and the immunofluorescence was even brighter after PTFCG treatment (with laser) because of the oxygen consumption by GOx catalysis and PDT. For comparison, the tumor hypoxia was effectively relieved after PTFCG@MH (plus laser) treatment, due to oxygenation by MnO<sub>2</sub>. From quantified results, the HIF-1 $\alpha$  level was decreased ~70% after PTFCG@MH treatment (Figure 5G). Therefore, the PTFCG@MH could effectively modulate tumor hypoxia microenvironment and provide O<sub>2</sub> substrate to improve PDT treatment outcome.

Finally, the biosafety of the nanosystem was examined. No obvious decrease of body weight was observed over the period of treatments (Figure S6), and the H&E staining showed no pathological change of the major organs after treatments (Figure S7). These results indicate the biocompatibility of the nanosystem for *in vivo* applications.

## Conclusions

In conclusion, an intelligent cyclic nano-reactor, PTFCG@MH, was fabricated for enhanced PDT against solid tumor. The nanostructure was well-characterized, and the cyclic reactions were explicitly demonstrated in solution, including GOx-catalyzed glucose consumption, MnO<sub>2</sub>-mediated oxygenation and GSH depletion. The surface HA modification endowed the nano-reactor with improved colloidal stability and active targetability to facilitate its accumulation into tumor after intravenous injection. After being delivered into tumor cells, PTFCG@MH boosted the PDT efficacy via simultaneous ATP/GSH suppression and self-oxygen supply, resulting in efficient tumor growth inhibition with no obvious side-effects. This cascade nano-reactor would promote the development of multifunctional nanoplatforms for improved cancer treatment by modulating unfavorable cancer microenvironment.

## Abbreviations

PDT: Photodynamic therapy; TME: tumor microenvironment; GOx: glucose oxidase; Ce6: chlorin e6; PLGA: poly (D, L-lactic-co-glycolic acid); MOF: metal-organic framework; HA: hyaluronic acid; GSH: glutathione; PSs: photosensitizers; ROS: reactive oxygen species; HIF-1 $\alpha$ : hypoxia inducible factor-1 $\alpha$ ; HSPs: heat shock proteins; P-gp: P-glycoprotein; ABCG2: ATP-binding cassette super-family G member 2; TA: Tannic acid; NR: Nile red; PAH: Poly (allylamine hydrochloride); SOSG: singlet oxygen sensor green; MTT: 3-(4, 5-

dimethylthiazol-2-yl)-2, 5-diphenyl tetrazolium bromide; DAPI: 4', 6-diamidino-2-phenylindole; NAC: N-acetylcysteine; DCFDA: 2' 7'-dichlorofluorescein diacetate; EDS: energy dispersive X-Ray spectroscopy; CLSM: confocal laser scanning microscopy;

## **Declarations**

### **Acknowledgments**

Not applicable.

### **Authors' contributions**

PL, JD, YL and WZ designed and conceptualized this study. PL, YZ and XS performed the in vitro and in vivo experiments. PL, YY, YP and QL drafted the manuscript. All of the authors have read and approved the final manuscript.

### **Funding**

This work was supported by Innovation-Driven Project of Central South University (No. 20170030010004), National Natural Science Foundation of China (No. 21804144, U1903125, 82073799).

### **Availability of data and materials**

All data generated or analysed during this study are included in this published article.

### **Ethics approval and consent to participate**

No applicable.

### **Consent for publication**

All authors agree to be published.

### **Competing interest**

The authors declare no conflict of interest.

## References

- (1) Dolmans, D.; Fukumura, D.; Jain, R. K. Photodynamic therapy for cancer. *Nat. Rev. Cancer* **2003**, 3, 380-387.
- (2) Li, X.; Kwon, N.; Guo, T.; Liu, Z.; Yoon, J. Innovative Strategies for Hypoxic-Tumor Photodynamic Therapy. *Angew Chem Int Edit* **2018**, 57, 11522-11531.
- (3) Xu, J.; Yu, S.; Wang, X.; Qian, Y.; Wu, W.; Zhang, S.; Zheng, B.; Wei, G.; Gao, S.; Cao, Z.; Fu, W.; Xiao, Z.; Lu, W. High Affinity of Chlorin e6 to Immunoglobulin G for Intraoperative Fluorescence Image-Guided Cancer Photodynamic and Checkpoint Blockade Therapy. *ACS Nano* **2019**, 13, 10242-10260.
- (4) Fan, W.; Huang, P.; Chen, X. Overcoming the Achilles' heel of photodynamic therapy. *Nat. Rev. Cancer* **2016**, 45, 6488-6519.
- (5) Wang, T.; Wang, D.; Yu, H.; Wang, M.; Liu, J.; Feng, B.; Zhou, F.; Yin, Q.; Zhang, Z.; Huang, Y.; Li, Y. Intracellularly Acid-Switchable Multifunctional Micelles for Combinational Photo/Chemotherapy of the Drug-Resistant Tumor. *ACS Nano* **2016**, 10, 3496-3508.
- (6) Yu, W. Q.; He, X. Q.; Yang, Z. H.; Yang, X. T.; Xiao, W.; Liu, R.; Xie, R.; Qin, L.; Gao, H. L. Sequentially responsive biomimetic nanoparticles with optimal size in combination with checkpoint blockade for cascade synergetic treatment of breast cancer and lung metastasis. *Biomaterials* **2019**, 217, 15.
- (7) Mahmoudi, K.; Garvey, K. L.; Bouras, A.; Cramer, G.; Stepp, H.; Raj, J. G. J.; Bozec, D.; Busch, T. M.; Hadjipanayis, C. G. 5-aminolevulinic acid photodynamic therapy for the treatment of high-grade gliomas. *J Neuro-Oncol* **2019**, 141, 595-607.
- (8) Alsaab, H. O.; Alghamdi, M. S.; Alotaibi, A. S.; Alzhrani, R.; Alwuthaynani, F.; Althobaiti, Y. S.; Almalki, A. H.; Sau, S.; Iyer, A. K. Progress in Clinical Trials of Photodynamic Therapy for Solid Tumors and the Role of Nanomedicine. *Cancers* **2020**, 12.
- (9) Aniogo, E. C.; George, B. P. A.; Abrahamse, H. The role of photodynamic therapy on multidrug resistant breast cancer. *Cancer Cell Int* **2019**, 19.
- (10) Liang, C.; Zhang, X. L.; Yang, M. S.; Wang, W. J.; Chen, P.; Dong, X. C. Remodeling Tumor Microenvironment by Multifunctional Nanoassemblies for Enhanced Photodynamic Cancer Therapy. *ACS Mater Lett* **2020**, 2, 1268-1286.
- (11) Fan, Y. T.; Zhou, T. J.; Cui, P. F.; He, Y. J.; Chang, X.; Xing, L.; Jiang, H. L. Modulation of Intracellular Oxygen Pressure by Dual-Drug Nanoparticles to Enhance Photodynamic Therapy. *Adv Funct Mater* **2019**, 29.

- (12) Dang, J.; He, H.; Chen, D.; Yin, L. Manipulating tumor hypoxia toward enhanced photodynamic therapy (PDT). *Biomater Sci* **2017**, 5, 1500-1511.
- (13) Cheng, X.; He, L.; Xu, J.; Fang, Q.; Yang, L.; Xue, Y.; Wang, X.; Tang, R. Oxygen-producing catalase-based prodrug nanoparticles overcoming resistance in hypoxia-mediated chemo-photodynamic therapy. *Acta Biomater.* **2020**, 112, 234-249.
- (14) Liu, P.; Xie, X.; Shi, X.; Peng, Y.; Ding, J.; Zhou, W. Oxygen-self-supplying and HIF-1 $\alpha$  Inhibiting Core-shell Nano-system for Hypoxia-resistant Photodynamic Therapy. *ACS Appl Mater Inter* **2019**, 11, 48261-48270.
- (15) Zeng, W.; Liu, P.; Pan, W.; Singh, S. R.; Wei, Y. Hypoxia and Hypoxia Inducible Factors in Tumor Metabolism. *Cancer Lett.* **2015**, 356, 263-267.
- (16) Meng, X.; Deng, J.; Liu, F.; Guo, T.; Liu, M.; Dai, P.; Fan, A.; Wang, Z.; Zhao, Y. Triggered All-Active Metal Organic Framework: Ferroptosis Machinery Contributes to the Apoptotic Photodynamic Antitumor Therapy. *Nano Lett.* **2019**, 19, 7866-7876.
- (17) Fuchs-Tarlovsky, V. Role of antioxidants in cancer therapy. *Nutrition* **2013**, 29, 15-21.
- (18) Chen, G.; Yang, Y. Y.; Xu, Q.; Ling, M. J.; Lin, H. M.; Ma, W.; Sun, R.; Xu, Y. C.; Liu, X. Q.; Li, N.; Yu, Z. Q.; Yu, M. Self-Amplification of Tumor Oxidative Stress with Degradable Metallic Complexes for Synergistic Cascade Tumor Therapy. *Nano Lett.* **2020**, 20, 8141-8150.
- (19) Thomas, A. P.; Lee, A. J.; Palanikumar, L.; Jana, B.; Kim, K.; Kim, S.; Ok, H.; Seol, J.; Kim, D.; Kang, B. H.; Ryu, J. H. Mitochondrial heat shock protein-guided photodynamic therapy. *Chem Commun* **2019**, 55, 12631-12634.
- (20) Zhao, L.; Li, J.; Su, Y.; Yang, L.; Chen, L.; Qiang, L.; Wang, Y.; Xiang, H.; Tham, H. P.; Peng, J.; Zhao, Y. MTH1 inhibitor amplifies the lethality of reactive oxygen species to tumor in photodynamic therapy. *Sci Adv* **2020**, 6.
- (21) Huo, D.; Jiang, X. Q.; Hu, Y. Recent Advances in Nanostrategies Capable of Overcoming Biological Barriers for Tumor Management. *Adv Mater* **2020**, 32, 28.
- (22) Han, H.; Hou, Y.; Chen, X.; Zhang, P.; Kang, M.; Jin, Q.; Ji, J.; Gao, M. Metformin-Induced Stromal Depletion to Enhance the Penetration of Gemcitabine-Loaded Magnetic Nanoparticles for Pancreatic Cancer Targeted Therapy. *J. Am. Chem. Soc.* **2020**, 142, 4944-4954.
- (23) Cheng, Y. H.; Cheng, H.; Jiang, C. X.; Qiu, X. F.; Wang, K. K.; Huan, W.; Yuan, A.; Wu, J. H.; Hu, Y. Q. Perfluorocarbon nanoparticles enhance reactive oxygen levels and tumour growth inhibition in photodynamic therapy. *Nat Commun* **2015**, 6, 1-8.

- (24) Liu, P.; Xie, X.; Liu, M.; Hu, S.; Ding, J.; Zhou, W. A smart MnO<sub>2</sub>-doped graphene oxide nanosheet for enhanced chemo-photodynamic combinatorial therapy via simultaneous oxygenation and glutathione depletion. *Acta Pharm Sin B* **2020**.
- (25) Chen, X.; Liu, Y.; Wen, Y.; Yu, Q.; Liu, J.; Zhao, Y.; Liu, J.; Ye, G. A photothermal-triggered nitric oxide nanogenerator combined with siRNA for precise therapy of osteoarthritis by suppressing macrophage inflammation. *Nanoscale* **2019**, 11, 6693-6709.
- (26) Zhang, Y.-H.; Qiu, W.-X.; Zhang, M.; Zhang, L.; Zhang, X.-Z. MnO<sub>2</sub> motor: A prospective cancer-starving therapy promoter. *ACS Appl Mater Inter* **2018**, 10, 15030-15039.
- (27) Lin, L.-S.; Song, J.; Song, L.; Ke, K.; Liu, Y.; Zhou, Z.; Shen, Z.; Li, J.; Yang, Z.; Tang, W.; Niu, G.; Yang, H.-H.; Chen, X. Simultaneous fenton-like ion delivery and glutathione depletion by MnO<sub>2</sub>-based nanoagent to enhance chemodynamic therapy. *Angew Chem Int Edit* **2018**, 57, 4902-4906.
- (28) Dong, Z.; Feng, L.; Chao, Y.; Hao, Y.; Chen, M.; Gong, F.; Han, X.; Zhang, R.; Cheng, L.; Liu, Z. Amplification of Tumor Oxidative Stresses with Liposomal Fenton Catalyst and Glutathione Inhibitor for Enhanced Cancer Chemotherapy and Radiotherapy. *Nano Lett.* **2019**, 19, 805-815.
- (29) Chen, Z.; Shi, T.; Zhang, L.; Zhu, P.; Deng, M.; Huang, C.; Hu, T.; Jiang, L.; Li, J. Mammalian drug efflux transporters of the ATP binding cassette (ABC) family in multidrug resistance: A review of the past decade. *Cancer Lett.* **2016**, 370, 153-164.
- (30) van Attikum, H.; Gasser, S. M. ATP-dependent chromatin remodeling and DNA double-strand break repair. *Cell Cycle* **2005**, 4, 1011-1014.
- (31) Liu, T.; Liu, W.; Zhang, M.; Yu, W.; Gao, F.; Li, C.; Wang, S.-B.; Feng, J.; Zhang, X.-Z. Ferrous-Supply-Regeneration Nanoengineering for Cancer-Cell-Specific Ferroptosis in Combination with Imaging-Guided Photodynamic Therapy. *ACS Nano* **2018**, 12, 12181-12192.
- (32) Liu, P.; Liu, X.; Cheng, Y.; Zhong, S.; Shi, X.; Wang, S.; Liu, M.; Ding, J.; Zhou, W. Core–Shell Nanosystems for Self-Activated Drug–Gene Combinations against Triple-Negative Breast Cancer. *ACS Appl Mater Inter* **2020**, 12, 53654-53664.
- (33) Stone, J. R.; Yang, S. Hydrogen peroxide: A signaling messenger. *Antioxid Redox Sign* **2006**, 8, 243-270.
- (34) Ding, B.; Shao, S.; Jiang, F.; Dang, P.; Sun, C.; Huang, S.; Ma, P. a.; Jin, D.; Al Kheraif, A. A.; Lin, J. MnO<sub>2</sub>-Disguised Upconversion Hybrid Nanocomposite: An Ideal Architecture for Tumor Microenvironment-Triggered UCL/MR Bioimaging and Enhanced Chemodynamic Therapy. *Chem Mater* **2019**, 31, 2651-2660.
- (35) Wan, S.-S.; Liu, M.-D.; Cheng, Q.; Cheng, H.; Zhang, X.-Z. A Mitochondria-Driven Metabolic Sensing Nanosystem for Oxygen Availability and Energy Blockade of Cancer. *Adv Ther* **2020**, 3.

(36) Ren, J.; Zhang, L.; Zhang, J.; Zhang, W.; Cao, Y.; Xu, Z.; Cui, H.; Kang, Y.; Xue, P. Light-activated oxygen self-supplied starving therapy in near-infrared (NIR) window and adjuvant hyperthermia-induced tumor ablation with an augmented sensitivity. *Biomaterials* **2020**, 234.

## Scheme

Scheme 1 is available in the Supplementary Files

## Figures

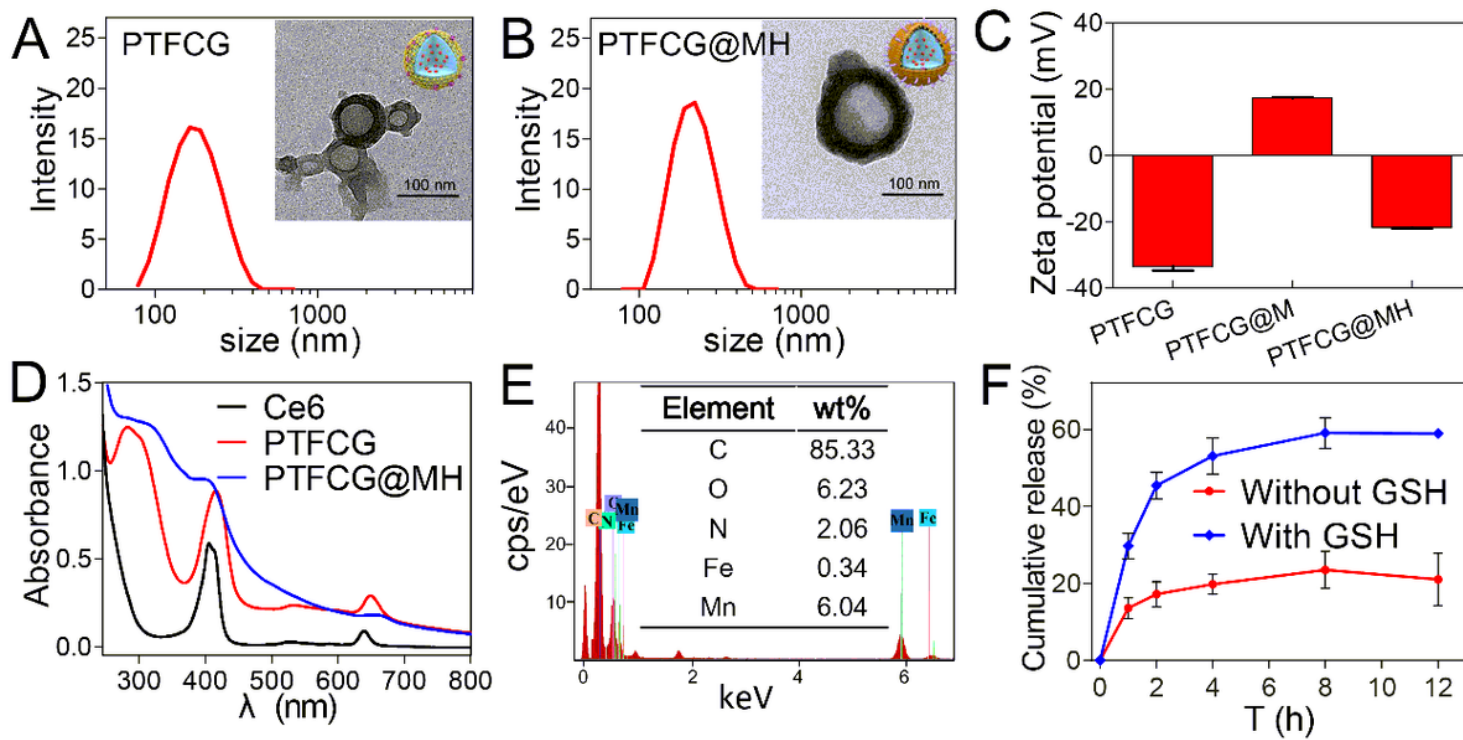


**Figure 1**

Dynamic sizes and TEM images of (A) PTFCG and (B) PTFCG@MH. (C) The  $\zeta$  potential of PTFCG, PTFCG@M and PTFCG@MH. (D) UV-vis absorbance spectra of Ce6, PTFCG and PTFCG@MH. (E) Energy dispersive X-Ray spectroscopy (EDS) analysis of PTFCG@MH. (F) In vitro Ce6 release from PTFCG@MH with or without addition of GSH (10 mM).

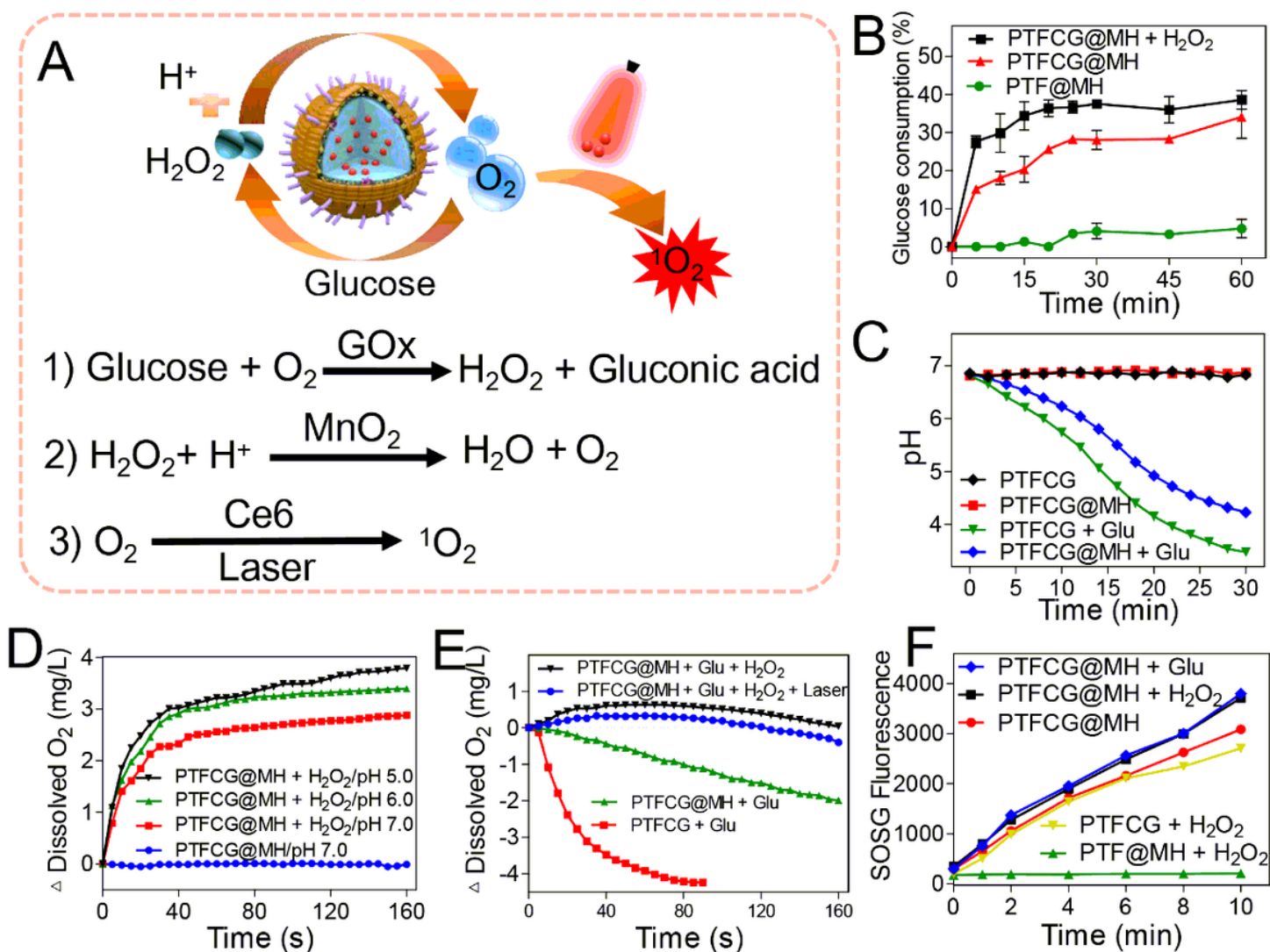


**Figure 2**

(A) Schematic illustration of cyclic reaction of PTFCG@MH. (B) Glucose consumption kinetics catalyzed by different formulations and conditions. (C) The kinetics of pH change for PTFCG@MH and PTFCG in absence or presence of glucose. (D) The kinetics of oxygen generation for PTFCG@MH in absence or presence of H<sub>2</sub>O<sub>2</sub> at different pH values. (E) Kinetics of dissolved oxygen variation for PTFCG@MH and PTFCG under different conditions. (F) The <sup>1</sup>O<sub>2</sub> generation kinetics for PTFCG@MH, PTFCG and PTF@MH in the presence or absence of H<sub>2</sub>O<sub>2</sub> or glucose under laser irradiation. The concentration of glucose and H<sub>2</sub>O<sub>2</sub> was 10 mM and 100 μM, respectively.

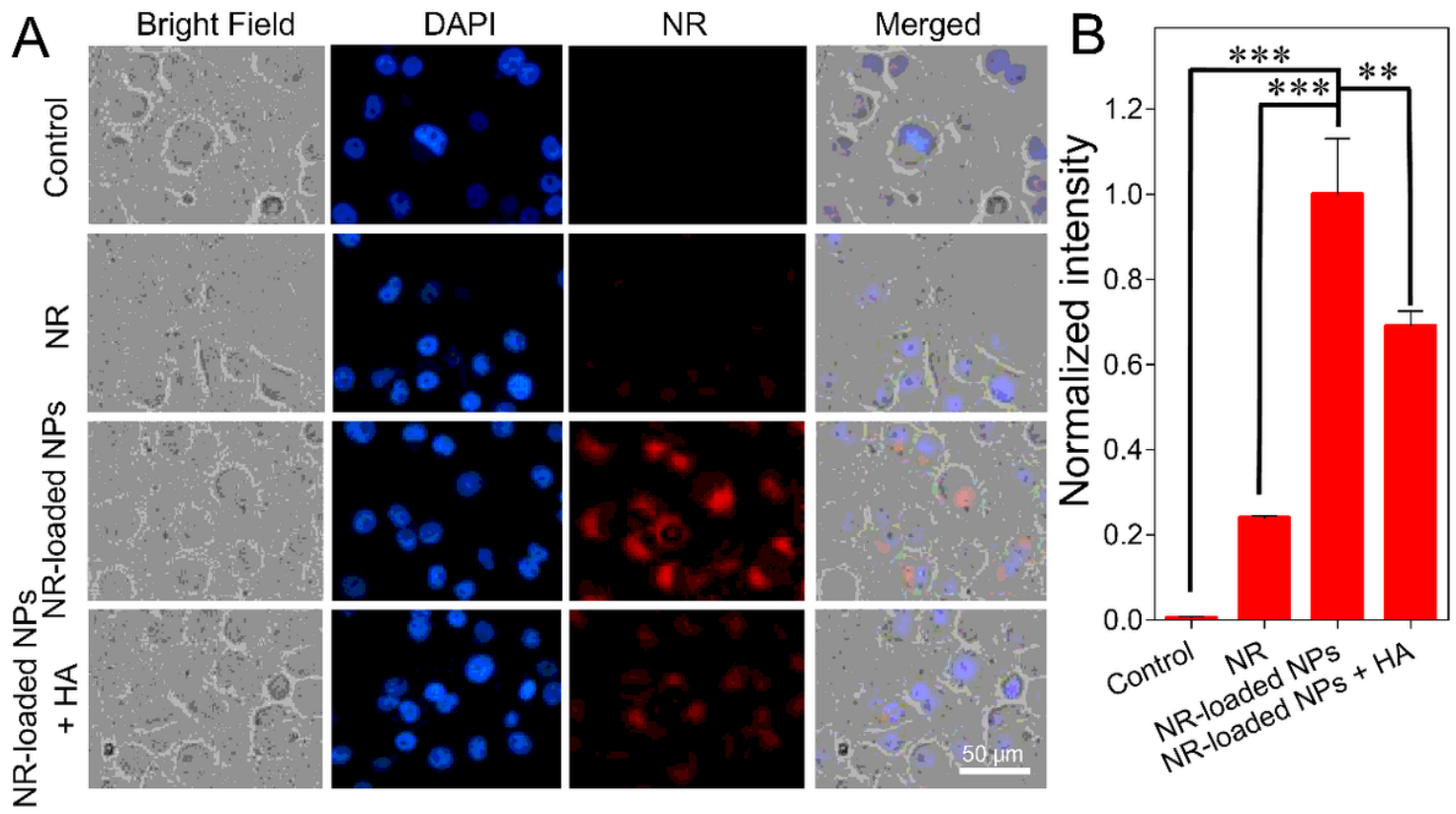


**Figure 3**

(A) Cellular uptake of free NR and NR-labeled PTFCG@MH measured by CLSM. (B) Intracellular fluorescence quantification for different groups. \*\*  $P < 0.01$ , \*\*\*  $P < 0.001$ .

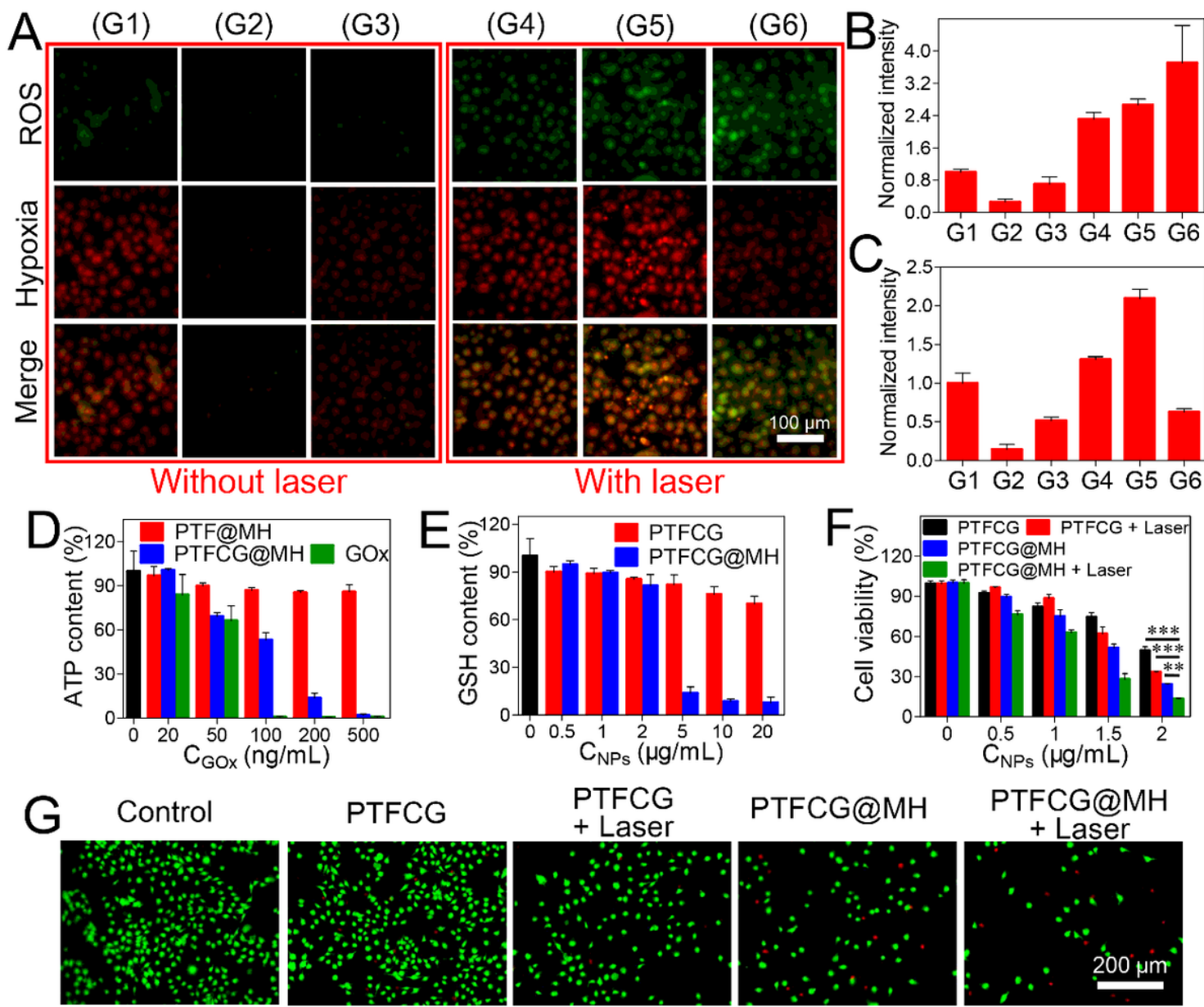


**Figure 4**

(A) Fluorescence images of intracellular ROS generation and hypoxia level with different treatments. The quantitative analysis of (B) ROS generation and (C) hypoxia level. In each panel, G1: Control; G2: PTF@MH; G3: PTFCG@MH; G4: Ce6 + Laser; G5: PTFCG + Laser; G6: PTFCG@MH + Laser. The intracellular (D) ATP and (E) GSH content of MDA-MB-231 cells incubated with various formulations. (F) Concentration dependent cytotoxicity of different formulations for MDA-MB-231 cells. (G) Fluorescence images of cells with different treatments after co-staining with calcein-AM and propidium iodide. \*\* P < 0.01, \*\*\* P < 0.001.

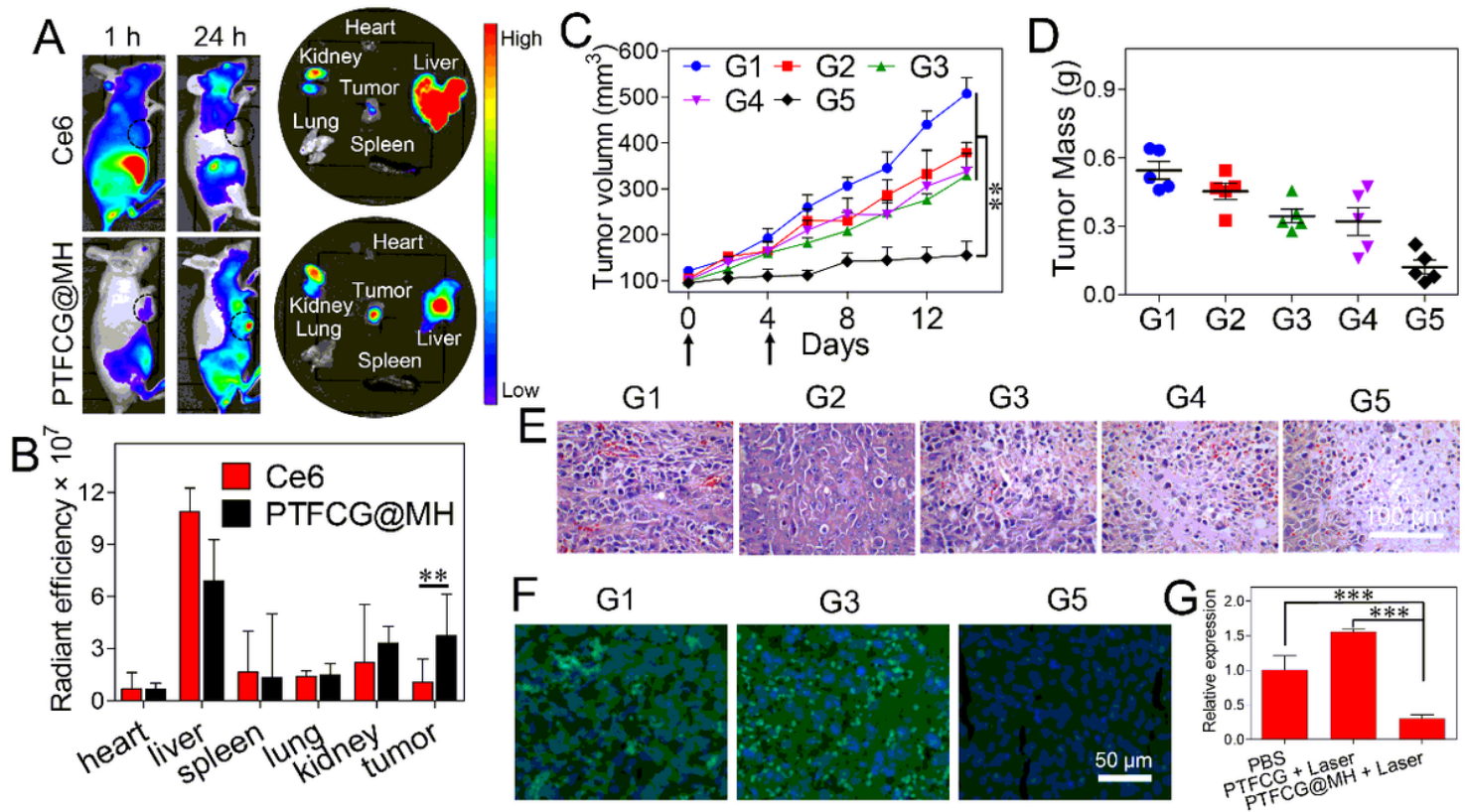


**Figure 5**

(A) In vivo (1 h vs 24 h post-injection) and ex vivo (24 h post-injection) fluorescent imaging of MDA-MB-231 tumor-bearing mice treated with free Ce6 and PTFCG@MH. (B) The quantified fluorescence intensity in major organs and tumor tissue at 24 h post injection. (C) Kinetics of tumor growth inhibition with various treatments. (D) Tumor mass and tumor images (inset) of the extracted tumor tissues after different treatments. (E) H&E staining and (F) HIF-1 $\alpha$  immunofluorescence staining of the tumor tissues with different treatments. (G) The quantified HIF-1 $\alpha$  level after different treatments. \*\*  $P < 0.01$ , \*\*\*  $P < 0.001$ . In each panel, G1: PBS; G2: Ce6 + Laser; G3: PTFCG + Laser; G4: PTFCG@MH; G5: PTFCG@MH + Laser.

## Supplementary Files

This is a list of supplementary files associated with this preprint. Click to download.

- [GraphicalAbstract.tif](#)
- [SupportingInformation1.docx](#)